X-ray investigation, high-resolution electron holography, and density functional calculations of single-crystalline $BaTiO_3$

A. Rother, M. Reibold, and H. Lichte
Triebenberg Laboratory, Institute of Structure Physics, Dresden University, D-01062 Dresden, Germany

T. Leisegang, A. A. Levin, P. Paufler, and D. C. Meyer
Institute of Structure Physics, Dresden University, D-01062 Dresden, Germany

S. Gemming
Institute of Ion Beam Physics and Materials Research, FZ Rossendorf, D-01314 Dresden, Germany

I. Chaplygin and G. Seifert
Institute of Physical Chemistry and Electrochemistry, Dresden University, D-01062 Dresden, Germany

A. Ormeci and H. Rosner
Max-Planck-Institute for Chemical Physics of Solids, 01187 Dresden, Germany

(Received 20 December 2005; revised manuscript received 2 August 2006; published 30 October 2006; corrected 29 November 2006)

Single crystal x-ray diffraction (XRD), high-resolution electron holography and density functional calculations (DFT) are employed to investigate single-crystalline $BaTiO_3$ in the noncentrosymmetric tetragonal phase. From XRD and DFT the structure parameters, the electron density and corresponding properties, such as atomic charges and the dipole moment are determined. For this purpose the maximum-entropy method was utilized to get accurate electron densities in the case of XRD, whereas all-electron calculations were performed in the framework of DFT. A comparison of experimental results and density functional calculations yield a rather good agreement. The electron density distributions are used to determine the "natural" unit cell corresponding to the neutral boundary cells of the whole crystal and its dipole moment, providing the boundary conditions necessary for calculating the electrostatic potential within the unit cell through the Poisson equation. The electrostatic potential was then utilized to perform electron scattering simulations within the framework of the Multislice formalism, resembling unique features of experimentally recorded electron holograms. It is shown that the phase wedge in the scattered wave, which is due to the polarization field within the specimen, is essential for the image reconstruction. This essential feature has not been included in simulations before.

DOI: 10.1103/PhysRevB.74.134116 PACS number(s): 77.84.Dy, 71.15.Mb, 61.10.Nz, 61.14.Nm

I. INTRODUCTION

$BaTiO_3$ is probably one of the most interesting members of the perovskite family, being mainly investigated for its electrical properties, since its discovery 50 years ago. It exhibits ferroelectric behavior at room temperature with a particularly high dielectric constant, making it a major constituent of ceramic capacitors and therefore of dynamic random access memories. Other applications are, for instance, thermistor or piezoelectric devices. Intensive investigations have been performed since the last century to determine and understand the structural and electrical properties of this material. Accurate structural parameters have been determined by several groups using x-ray or neutron diffraction techniques.[1–3] Comprehensive *ab initio* calculations have been conducted by, for example, Cohen and Krakauer[4] and King-Smith and Vanderbilt.[5] It could be verified that $BaTiO_3$ is a polymorph, which exhibits four different structural phases, with only slightly differing structural parameters. Furthermore the macroscopic behavior of $BaTiO_3$ at room temperature reveals many interesting features, especially the formation of ferroelectric domains and domain walls.[6–8] It is particularly difficult to produce single domain crystals big enough for the investigation by x-ray diffraction techniques. In this work single domain properties of noncentrosymmetric tetragonal $BaTiO_3$ with space group symmetry (99) $P4mm$ (Fig. 1), namely the structural parameters and the electron density (ED), were investigated using both, density-functional-theory (DFT) calculations and single crystal x-ray diffraction (XRD) analysis.

The agreement of the results obtained by both methods was evaluated. The simulated ED was then investigated to obtain the natural unit cell (i.e., an unit cell corresponding to the neutral boundary cells of the whole crystal) and hence to calculate the dipole moment. Consequently the electrostatic potential could be determined by solving the Poisson equation for the simulated ED with the boundary conditions fixed by the natural unit cell. The electrostatic potential is the essential feature for electron scattering experiments, which offer a further possibility to determine the structure of $BaTiO_3$ and other structures in general. We compared electron scattering simulations, using the Multislice algorithm with images recorded with the technique of high-resolution electron holography to test our results for the potential obtained. Particularly the potential wedge produced by the polarization field could be observed in the phase of both, the reconstructed waves and the simulated waves. High-resolution electron microscopic imaging simulations until now could not reproduce this feature.

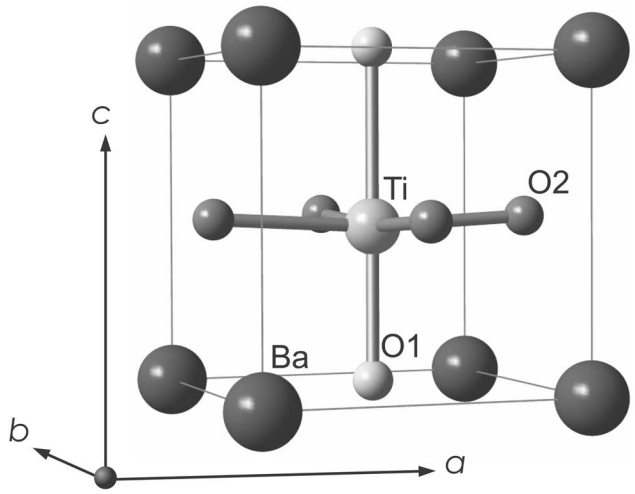

FIG. 1. Scheme of the unit-cell of tetragonal $BaTiO_3$ [a =3.9946(2) Å, c=4.0388(5) Å], noncentrosymmetric space-group (99) $P4mm$, with tetragonal distortion pointing along c direction.

II. EXPERIMENTAL INVESTIGATIONS

A. Single crystal x-ray diffraction

To make a detailed comparison of experimental and theoretical approaches, a complete data set of x-ray reflection intensities was recorded using a single-crystal XRD technique. For the comparison both, structural parameters and experimental structure factors are necessary to resolve small features within the ED maps.

1. Preparation and measurement

From a single-crystalline $BaTiO_3$ wafer (Crystec GmbH; one side polished) a single crystal ($0.08\times0.08\times0.04$ mm^3, transparent, flat) was cut out and mounted on a sharpened glass fibre (diameter of ~100 μm). The XRD measurement (resolution up to $\sin\theta/\lambda=1.1$ Å^{-1}) was performed at ambient conditions (T=303 K) using a STADI4 diffraction system[9] with Mo-Kα radiation ($\lambda_{\text{Mo-K}\alpha}$=0.71069 Å). After data collection, a numerical absorption correction (linear absorption coefficient μ_l=18.01 mm^{-1}) was carried out by means of the programs XRED and XSHAPE (Refs. 10 and 11) and applied to the 2734 reflections measured (R_{int} =4.87%).

2. Structure refinement

Before the structure refinement, the unit cell parameters were refined confirming a tetragonal unit cell [a =3.9946(2) Å, c=4.0388(5) Å]. In comparison with the data of Buttner and Maslen,[3] the unit-cell parameters are smaller by about 0.1% in a direction and larger by about 0.5% in c direction, resulting in an increased unit-cell volume [V =64.45(1) Å^3] and a stronger tetragonal distortion of the unit cell for the crystal investigated. The starting atomic coordinates for the structure refinement of the $BaTiO_3$ single crystal were taken from the work of Buttner and Maslen.[3] The refinement was performed with the crystallographic computing system JANA2000.[12] Two possible tetragonal space groups, (99) $P4mm$ (noncentrosymmetric) and (123) $P4/mmm$ (centrosymmetric) were tested and the structure parameters as well as the quality parameters were compared. Taking into account the smaller values of the thermal displacement parameters U_{33} of the O and Ti atoms along c axis and the quality parameters of the refinement [R_1=1.65%, wR_2=4.65% and S=1.20 for 442 independent reflection with $I>3\cdot\sigma(I)$] the data are consistent with the noncentrosymmetric space group (99) $P4mm$ in agreement with Buttner and Maslen.[3] Additionally, different types of twinning were tested with no significant improvement of the structure model (changes are smaller than $1\cdot\sigma$) and, consequently, of the calculated remaining ED (see the next section). The variation of the site occupancy values gave no significant deviations from unity (deviations are less than $0.5\cdot\sigma$).

Thus, from the viewpoint of XRD, the single crystal investigated consists of one structural domain with no oxygen and cation deficiency. The final structure model parameters obtained by refinement are summarized in Table I. Large correlations of refinement parameters were found for z_{Ti}/U_{33}(Ti) (0.97), z_{O1}/U_{33}(O1) (−0.904), z_{O2}/U_{33}(O2) (−0.858).

3. Electron density determination from the XRD data by the maximum entropy method

We used the BayMEM software package to calculate the ED by the maximum entropy method (MEM).[13] This method is based on the maximization of the entropy functional S while certain constraints are fulfilled. For details see, for example, Gilmore (1996).[14] The entropy is defined as

$$S=-\sum_{i=1}^{N_p}\rho_i\cdot\log\frac{\rho_i}{\tau_i}, \tag{1}$$

where ρ_i is the ED on the grid point N_i of a grid with N_p $=N_1\times N_2\times N_3$ grid points and τ_i is the prior or reference ED

TABLE I. Final fractional atomic coordinates x, y, z and anisotropic thermal displacement parameters U_{ij} of the atoms of tetragonal $BaTiO_3$ [space group (99) $P4mm$] obtained by structure refinement using singe-crystal x-ray data. The estimated standard deviations (e.s.d.) are shown in brackets.

Atom	Wyckoff site	x/a	y/b	z/c	U_{11} (Å^2)	U_{22} (Å^2)	U_{33} (Å^2)
Ba	1a	0	0	0	0.0056(1)	U_{11}	0.0063(1)
Ti	1b	1/2	1/2	0.4883(18)	0.0076(1)	U_{11}	0.0076(8)
O1	1b	1/2	1/2	0.0247(23)	0.0077(5)	U_{11}	0.0055(25)
O2	2c	1/2	0	0.5139(27)	0.0074(5)	0.0067(5)	0.0086(11)

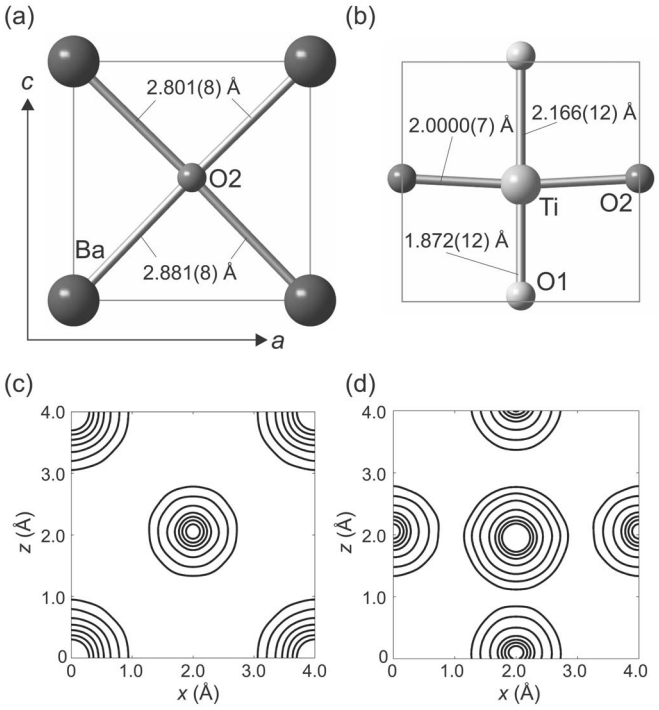

FIG. 2. A scheme of the section of (010) lattice plane at $y=0$ (a) and $y=0.5$ (b) according to results of structure refinement by means of XRD analysis are drawn. The atomic distances calculated from structure model (Table I) are indicated. ED maps of the corresponding crystal planes obtained by XRD analysis are shown in (c) and (d). The contour lines characterizing constant positive ED are drawn at $\rho=2^n\ e/\text{Å}^3\ n\in\{0,1,\ldots,6\}$. A shift of the Ti and O atoms along c (i.e., z) direction can clearly be seen.

in this point. This method allows a very accurate reconstructing of the optimum ED from experimental data without correlations of parameter (see Sec. II A 3). A prior derived ED was used to study fine features of ED such as atomic charges or the distribution of bonding electrons.[15,16] An accurate prior density can be obtained from a standard structure refinement within the approximation of the independent atom model (IAM). In this model the ED distribution is calculated as a superposition of the ED of free, noninteracting atoms placed at their refined positions and convoluted with their thermal motion. Structure parameters obtained by refinement (Table I) were utilized for the calculation of the prior density of one unit cell and sampled on a $128\times128\times128$ pixel grid being much larger than the experimental sampling rate obtained by the measurement (which is around $12\times12\times12$, see Sec. II A 1). The algorithm used for calculating the prior density fills up the nonmeasured reflections in Fourier space analytically according to the sampling rate chosen. Hence, no termination errors are introduced by the analytical Fourier transformation.[16] The ED distribution of $BaTiO_3$ was calculated using the Sakata and Sato algorithm.[17] After final iteration cycle the ED converged to values $R_1=1.44\%$ and $wR_1=1.97\%$. In Fig. 2 the ED $\rho(\mathbf{r})$ calculated from x-ray experimental data, including the thermal smoothing, is shown for two sections of the unit cell [(010) plane with $y=0$ (a) and $y=0.5$ (b)] which are mirror planes of the tetragonal structure. On base of the structure parameters refined (Table I), corresponding lattice planes are schematically drawn and the atomic distances are indicated.

B. HRTEM

High-resolution electron microscopy (HRTEM) offers another possibility to determine structural parameters. The electrons used are usually high energy electrons. They are scattered by the electrostatic potential $U(\mathbf{r})$ of the specimen, since scattering of electrons is governed by the Dirac equation containing the electrostatic potential in the Hamiltonian. Thus, one can say that x-ray techniques are probing the electron density $\rho(\mathbf{r})$, whereas electron scattering techniques are probing the Coulomb potential $U(\mathbf{r})$. In particular the convergent beam electron diffraction (CBED) method is used to determine the space group symmetry of small volumes of the crystal.[18] In the case of $BaTiO_3$, the space group of tetragonal structure [(99)$P4mm$] investigated here was first determined with CBED by Tanaka and Lehmpfuhl.[19] This method is also capable of mapping the potential distribution inside the specimen by comparing the measured electron diffraction data with simulated data, followed by a refinement procedure. Other electron beam techniques, used to map potential distributions, are high-resolution methods using parallel illumination of the specimen.[20] Particularly high-resolution electron holography using a two dimensional detector (e.g., CCD-Camera) can record both amplitude $A(\mathbf{R})$ and phase $\phi(\mathbf{R})$ of the electron wave $\Psi(\mathbf{R})=A(\mathbf{R})e^{i\phi(\mathbf{R})}$. The phase $\phi(\mathbf{R})$ obeys under certain circumstances (basically the applicability of small angle scattering approximation and a relativistic correction) a direct dependency on the projected potential[20]

$$\phi(\mathbf{R})=\sigma\int_d U(\mathbf{R},y)dy. \tag{2}$$

Here σ is a constant, d is a line through the specimen parallel to the electron beam (y axis in this case), and $\mathbf{R}$ denotes a two-dimensional vector in the (xz) plane perpendicular to the y axis. The refinement methods used for electron diffraction are based on accurate numerical models of the scattering experiment. In particular they depend on the accuracy of the used electrostatic potentials. From data sets of the electron density one can calculate the electrostatic potential by solving the Poisson equation

$$\Delta U(\mathbf{r})=-\frac{1}{\epsilon_0}\rho(\mathbf{r}) \tag{3}$$

within certain boundary conditions. The potential $U(\mathbf{r})$ generally consists of two parts $U(\mathbf{r})=\tilde{U}(\mathbf{r})+U_h(\mathbf{r})$: The first part is the particular solution and it is periodic, due to the perfect periodicity of the ED. Consequently, it can be conveniently calculated in the Fourier space

$$\tilde{U}(\mathbf{g})=\frac{\rho(\mathbf{g})}{4\pi^2\epsilon_0|\mathbf{g}|^2}. \tag{4}$$

The value $\tilde{U}(\mathbf{g})$ at $|\mathbf{g}|^2=0$ in (4) is not determined, which corresponds to the free choice of a potential offset in an

infinite system, where no gauge level (such as vacuum) is present. The second part is a harmonic function, i.e., $\Delta U_h(\mathbf{r})=0$, which is determined by the boundary conditions. For a three-dimensional infinite periodic crystal, consisting of unit cells without dipole moment

$$\mathbf{p} = \int_V \rho(\mathbf{r}) \cdot \mathbf{r} d^3 r, \tag{5}$$

$U_h(\mathbf{r})$ is a constant, whereas unit cells possessing a nonvanishing dipole moment produce a potential wedge, directly related to the polarization field by the path integral

$$U_h(\mathbf{r}) = -1/\epsilon_0 \int_{-\infty}^{\mathbf{r}} \mathbf{p}(\mathbf{r}')/V \cdot d\mathbf{r}'. \tag{6}$$

In a finite system the value $U_h(\mathbf{r})$ is well defined by (6), if the unit cell determining $\mathbf{p}$, is chosen such that, the boundary cells of the whole crystal are neutral. This special choice for the unit cell is called a "natural" unit cell.[21] The same holds when going to infinity, except that an arbitrary constant can now be added to $U_h(\mathbf{r})$, which is again due to a missing gauge level in an infinite system. An alternative approach to the determination of $U_h(\mathbf{r})$ would include a choice of a unit cell with zero dipole moment and therefore charged boundary cells in the case of a polarized system. Due to the $1/r$ dependency, electrostatic potentials of atoms are strongly divergent in the vicinity of the atom cores. This divergent region close to the atom cores is responsible for most of the features of electron scattering. It is therefore crucial to have a high sampling rate of the potential to describe the divergence sufficiently in electron scattering simulations.[22] Clearly, via DFT calculated densities (Sec. II C) provide a better basis for the accurate determination of the potentials in this case, since their sampling rate is only limited by computational power, whereas the experimental determination of high-angle reflections is severely limited by their low intensity and has to be extrapolated by modeling anyway.

C. Density functional calculations

Density-functional[23,24] band-structure calculations were employed to obtain the structural and electronic properties of the cubic and tetragonal structures of $BaTiO_3$ within the local density approximation (LDA) and the generalized gradient approximation (GGA). A structure optimization was carried out with the program package ABINIT,[25] employing a plane-wave basis with a cutoff energy of 1333 eV to represent the valence and semicore electrons (Ba: $5p^6 6s^2$, Ti: $3p^6 4s^2 3d^2$, O: $2s^2 2p^4$) and soft-core pseudopotentials for the atom cores.[26] For the investigation of tetragonal $BaTiO_3$, the c/a ratio was kept fixed at the experimental value of 1.011, obtained by the XRD. The optimized tetragonal and cubic structures are almost isoenergetic with the tetragonal one being less than 10 meV lower in energy, which is in an excellent agreement with previous calculations on distorted $BaTiO_3$ phases.[27] Optimization of the structural parameters yielded lattice parameters (a_{LDA} =3.994 Å, c_{LDA}=4.038 Å and a_{GGA}=4.004 Å, c_{GGA} =4.049 Å) similar to those obtained by the XRD (Sec. II A 1). The values calculated by the GGA functional are higher than the LDA-calculated ones, in agreement with the well- known behavior that in the GGA the gradient terms tend to correct the over binding nature of the LDA. This tendency can be related to the fact that in the GGA calculations ED near the atomic nuclei are slightly higher (see Sec. III A). The atomic positions, calculated by the DFT within the LDA (GGA in parentheses), are listed in Table II, and selected lattice planes of the unit cell are schematically shown in Fig. 3. The differences in the internal coordinates optimized by the LDA and the GGA calculations are negligible in the sense that they do not affect the results in any way.

TABLE II. Fractional atomic coordinates of tetragonal $BaTiO_3$ [space group (99) $P4mm$] obtained by DFT LDA (GGA) calculations. The e.s.d.'s are evaluated to be in the order of 1%.

Atom	x/a	y/b	z/c
Ba	0	0	0
Ti	1/2	1/2	0.483 (0.487)
O1	1/2	1/2	0.027 (0.023)
O2	1/2	0	0.513 (0.513)

A more accurate computation of the electron density was performed for the tetragonal phase only, since for this crys-

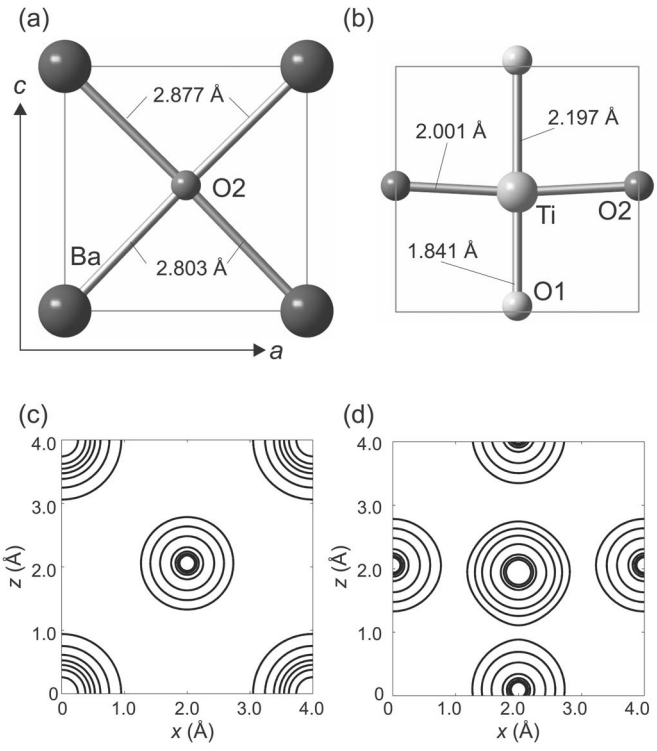

FIG. 3. A scheme of the section of (010) lattice plane at $y=0$ (a) and $y=0.5$ (b) according to results of structure optimization by DFT (LDA) calculations are drawn. The atomic distances calculated from structure model (Table II) are indicated. ED maps of the corresponding crystal planes obtained by DFT (LDA) calculations are shown in (c) and (d). The contour lines characterizing constant positive ED are drawn at $\rho=2^n\ e/\text{Å}^3$ $n \in \{0,1,\ldots,6\}$. Again, the shift of the Ti and O atoms along c direction can clearly be seen.

TABLE III. Difference of structure parameters (<1%) obtained by DFT (LDA) calculations and XRD analysis.

$a_{LDA}-a_{XRD}$ (Å)	−0.001
$(z_{Ba}/c)_{LDA}-(z_{Ba}/c)_{XRD}$	0
$(z_{Ti}/c)_{LDA}-(z_{Ti}/c)_{XRD}$	−0.005
$(z_{O1}/c)_{LDA}-(z_{O1}/c)_{XRD}$	0.002
$(z_{O2}/c)_{LDA}-(z_{O2}/c)_{XRD}$	−0.001

TABLE IV. Shifts of the Ti and O1 atoms within the noncentrosymmetric $BaTiO_3$ unit cell relative to the ideal positions of the centrosymmetric structure.

	Δz_{Ti} (Å)	Δz_{O1} (Å)	Δz_{O1} (Å)
XRD	0.047(7)	0.100(9)	0.056(11)
DFT (LDA)	0.069	0.109	0.052
Buttner *et al.*[3]	0.072(4)	0.064(20)	0.060(12)

talline polymorph modification of $BaTiO_3$ the XRD measurements have been performed. The ED was calculated using the all-electron full-potential local-orbital (FPLO, version 4.00-16) calculation scheme.[28] The calculations were scalar relativistic.[29] For comparison two versions of the exchange-correlation functional were used: The Perdew-Wang parametrization[30] of the LDA exchange-correlation functional and the Perdew-Burke-Ernzerhof[31] parametrization of the GGA exchange-correlation functional.[32] The local orbital basis set (Ba: $5s5p/4f5d6s6p$, Ti: $3s3p/3d4s4p$, O: $-/2s2p3d$) of semicore/valence atomic orbitals was chosen. As the core states are solutions of the Dirac equation assuming a point-charge electrostatic potential of nuclei, the "on-site" electron density diverges at the atom sites and this (infinite) contribution was omitted at the grid points coinciding with an atom position. The ED shown in Fig. 3 has been computed within the LDA and on a $128\times128\times128$ grid of one unit cell. Additionally the thermal averaging was applied, using an average value for each direction of the mean square displacements listed in Table I.

III. COMPARISON

A. Structure parameters and electron densities

In this section, the results, obtained by the above-described methods, are discussed. First, the structure parameters are compared. As mentioned above, the c/a ratio was not determined via DFT but taken from the XRD investigation, so that the unit cell dimensions as well as the displacement of the atoms were calculated only. They are in an excellent agreement with the parameters obtained by the XRD refinement (see Table III). The differences are smaller than 1%.

The largest difference of ~0.02 Å is showing up at the position of the titanium atom, which, nevertheless, lies well in the range of the e.s.d.'s of the applied methods. Therefore, the relaxation of the atom positions in the framework of DFT applied to valence and semicore states proves to be very accurate in the case of $BaTiO_3$. Vice versa, the same statement holds for the refinement method applied to the XRD data. When comparing the displacements from the ideal positions (centrosymmetric structure) in z direction it can be seen that, the O1 atoms exhibit a larger shift than the Ti atoms (Table IV), which is the case for both, the XRD and DFT data.

The ED densities obtained within the GGA and the LDA approximations showed only negligible relative deviations being maximally of the order of 0.1% in the vicinity of the atom cores. This finding collaborates well with the general observation that GGA calculations yield higher ED values near the nuclei. Because the LDA-GGA differences in the ED are small, the ED computed within the LDA will be referred to as the "theoretical result" in the following discussions and analyses. Figure 4 shows the difference density $\rho_{dif}=\rho_{LDA}-\rho_{XRD}$ depicted for the selected (010)-planes, the experimental and theoretical densities are depicted in Figs. 2 and 3, respectively.

The ED calculated by both, DFT and XRD agree excellently, considering the amplitude of the deviations depicted. Beside of the differences at the atom positions, which are due to the different thermal averaging in the MEM ED (each atom is averaged differently) and the DFT ED (all atoms are averaged identically), one observes a stronger asymmetry of the DFT densities in particular for the Ti-O1 bond. Since the shifts of the atoms correspond very well for the two methods, one can ascribe this effect on the one hand to the independent atom model used for the refinement of XRD intensities and on the other hand to local polarizations (overestimated local dipole moment) in the DFT calculations (see the next section).

B. Atomic charges and dipole moment

Another view at the atomic bonding is provided by a Bader analysis,[33] which yields a static charge distribution of the atoms by topological arguments, a measure comparable to the valence of the atoms within the structure. The Bader charges calculated from MEM ED of XRD data and DFT ED respectively are shown in Table V.

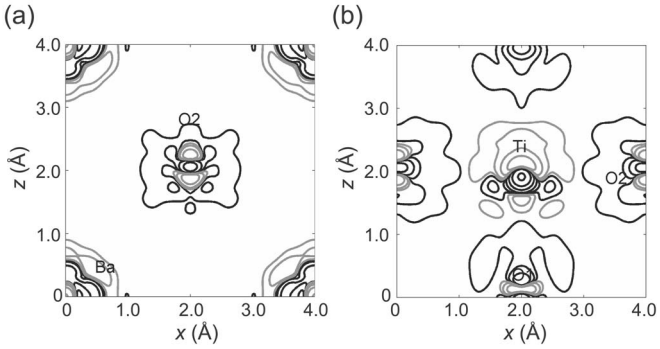

FIG. 4. ED difference maps ($\rho_{dif}=\rho_{LDA}-\rho_{XRD}$) of (010)-crystal plane at $b=0$ Å (i.e., $y=0$) (a) and $b=1.997$ Å ($y=0.5$) (b). The black contour lines characterizing constant positive differences are drawn at $\rho=2^n\ e/\text{Å}^3\ n\in\{-2,-1,\ldots,4\}$. The gray lines characterizing negative differences at the same values.

TABLE V. Atomic (valence) charges according to Bader (Ref. 33) obtained by DFT (LDA) calculations and MEM analysis of XRD data.

	XRD	DFT (LDA)
ρ_{Ba} (ρ_{Ba}-$\rho_{Ba,0}$)	55.2 (0.8)	54.68 (1.32)
ρ_{Ti} (ρ_{Ti}-$\rho_{Ti,0}$)	20.6 (1.4)	19.98 (2.02)
ρ_{O1} (ρ_{O1}-$\rho_{O1,0}$)	8.8 (−0.8)	9.08 (−1.08)
ρ_{O2} (ρ_{O2}-$\rho_{O2,0}$)	8.7 (−0.7)	9.13 (−1.13)

As assumed, the valence of Ti is the highest of all constituents, emphasizing again the strong Ti-O bonding. Furthermore, the atomic charges calculated from MEM ED of XRD are always closer to the neutral atomic charges then the DFT ones, which is possibly again due to the argument listed at the end of the preceding section. Additionally, the Bader analysis of the DFT ED can be utilized to get more accurate atomic scattering amplitudes including bonding effects replacing the IAM currently used. However, this approach is still under development. Since tetragonal $BaTiO_3$ exhibits ferroelectric behavior the spontaneous polarization is an essential parameter describing the electric properties of the material. The calculation of the dipole moment requires the determination of the natural unit cell. We therefore again performed a Bader analysis for all atoms within one unit cell. Connecting all nonadjacent atomic Bader surfaces one gets the surface of the natural unit cell. This is because in our case the Bader surfaces actually connect the points with minimum charge density and therefore approximate the termination of the crystal to vacuum. Two possible choices for the termination in z direction are possible however. We placed the cut between the long Ti-O bonding, being slightly more stable than the short one. The dipole moment was evaluated to 0.04 e nm (XRD) and 0.18 e nm (DFT, both LDA and GGA), which is significantly higher. Experimental values are reported to be around $0.1e$ nm.[34] As already mentioned we ascribe this overestimation partially to a compensation of the polarization field in the DFT calculation due to the periodic boundary conditions employed in the calculations. Nevertheless, the periodic boundary conditions do not hold in the case of polarized materials, due to the potential wedge introduced by the polarization field of a finite crystal. Different approaches to solve that problem are presented for example by Ghosez.[35] The underestimation of the dipole moment in the case of XRD measurements can be ascribed to the independent atom model, damping the redistribution of the electrons due to bonding effects.

C. Electrostatic potential

The potential calculated on the basis of the DFT electron densities via Eq. (3) is depicted in Fig. 5. It can be seen that the redistribution of the valence electrons (e.g., Fig. 4) produces a comparably small deformation of the nearly spherical atomic potentials in the vicinity of the atoms, which, to a good approximation, occur in the case of free atoms (dotted lines in Fig. 6 represent isolated atomic potentials from Weickenmeier and Kohl[36]).

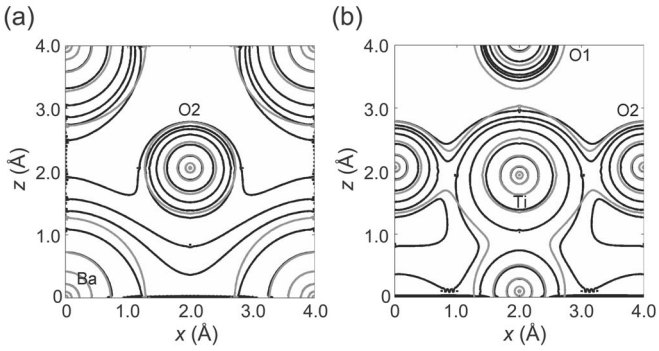

FIG. 5. Potential maps of the (010) crystal planes at (a) $y/b=0$ and (b) $y/b=0.5$. The black contour lines are drawn at $U=4^nV$ $n\in\{0,1,\ldots,5\}$. The gray lines represent an artificial $BaTiO_3$ lattice consisting of free atoms.

In contrast to the small deformation of the atomic potentials, one can readily see the shift of the Ti and O atoms and the potential wedge due to polarization. Therefore, the questions arise, whether it is possible to measure redistributions of valence electrons by means of high-energy electron diffraction, and whether it is necessary to include them into the simulations of the electron scattering. The electrostatic potential shown in Fig. 6 is currently used to calculate high-resolution electron holograms by means of multislice methods,[37] which combine the effect of the electrostatic potential (2) and the propagation of the electron waves to extend the applicability of Eq. (2). One typical result is shown in Fig. 6(a). Here the influences of the microscope (such as lens aberrations, camera distortions, etc.) have been incorporated. It is again mentioned, that the linear growth in the

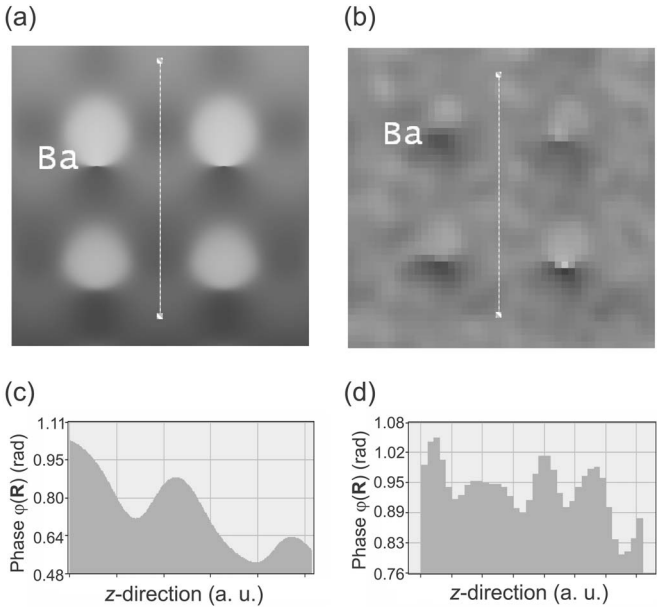

FIG. 6. Phase of an object exit wave of one unit cell simulated with the EMS software (a) and recorded experimentally by means of electron holography (b). Influences of the microscope (e.g., lens aberrations, camera distortions) have been incorporated in the simulation. Selected line scans of (a) and (b) are depicted in (c) and (d) respectively, revealing the phase wedge.

phase occurs, due to the incorporation of polarization in the calculation of the potential. One can now basically compare this simulated image with the one obtained by high-resolution electron holographic measurements [Fig. 6(b)], and vary the parameters of the potential and simulation model to fit the experimental results. One can readily see the phase wedge due to the polarization, although the field of view is very small. Generally the phase shift in high-resolution images is lower than the predicted one, since size effects, which attenuate the polarization in thin crystal regions used for imaging, play a role. Unfortunately, the presence of the potential wedge complicates the refinement, especially the correction of lens aberrations, since the modulation of the electron wave by lens aberrations is much more involved, i.e., large amplitude or phase contrasts do not necessarily occur at atom positions anymore. This effect can be seen readily in Fig. 6, where a bright-dark switch is visible at the Ba site, which would not occur in the case of the non-polarized centrosymmetric structure. The dipole character of tetragonal $BaTiO_3$ can be revealed more conveniently by means of medium-resolution electron holography.[38] According to the linear growth of the potential in the direction of polarization one can measure a much stronger phase shift over large field of views, i.e., in the medium resolution mode.

IV. SUMMARY

We have presented a comparative study of $BaTiO_3$ using x-ray diffraction analysis, LDA and GGA based first-principles calculations and high-resolution electron holography to reveal the influence of certain features of electron density distributions as, for example, the potential wedge introduced by a polarization of a unit cell. Particularly the last point has a strong impact on calculations of the electrostatic potential and therefore by the multislice method simulated high-resolution electron transmission holographic images as was pointed out. A detailed comparison of the experimental and theoretical densities yields an excellent agreement of the structure parameters (less than 1% differences) of the $BaTiO_3$ perovskite. The quantitative comparison of the electron densities yields significant differences only in integrated properties, such as the static atomic charges and the dipole moments. From the accurate ED of the DFT calculations the electrostatic potentials have been calculated, including the potential wedge introduced by the polarization field. Scattering simulations based on these electrostatic potentials agree well with experimentally recorded images by means of high-resolution electron holography, giving another basis for the verification of the calculated electron densities and their dipole moments. It could be verified, that the dipole moment of the thin regions of the crystal used for the imaging is lower than the bulk value. Furthermore the similarity between isolated and bonded atom potentials shows that the electrostatic potentials of the atoms are not significantly affected by redistribution of valence electrons in the case of $BaTiO_3$. It is the atom positions and the potential wedge, which play a crucial role for electron scattering in this case. We can summarize that both, XRD measurements and DFT calculations yield accurate atom positions, electron densities and dipole moments, which can be used to set up more precise refinement models for both, XRD and HRTEM.

ACKNOWLEDGMENTS

We thank L. Palatinus for helpful discussion and support on BayMEM. The financial support by FOR 520 is gratefully acknowledged. The research of A.O. and H.R. is supported by the DFG Emmy Noether program. A.O. and H.R. are thankful to Xianlong Wang for testing the new GGA implementation in FPLO extensively.

[1] B. C. Frazer, H. R. Danner, and R. Pepinski, Phys. Rev. **100**, 745 (1955).
[2] H. T. Evans, Jr., Acta Crystallogr. **14**, 1019 (1961).
[3] R. H. Buttner and E. N. Maslen, Acta Crystallogr. **48**, 764 (1992).
[4] R. E. Cohen and H. Krakauer, Phys. Rev. B **42**, 6416 (1990).
[5] R. D. King-Smith and D. Vanderbilt, Phys. Rev. B **49**, 5828 (1994).
[6] V. A. Zhirnov, Zh. Eksp. Teor. Fiz. **35**, 1175 (1958) [Sov. Phys. JETP **35**, 822 (1959)].
[7] J. Padilla, W. Zhong, and D. Vanderbilt, Phys. Rev. B **53**, R5969 (1996).
[8] F. Tsai, V. Khiznichenko, and J. M. Cowley, Ultramicroscopy **45**, 55 (1992).
[9] STOE and Cie GmbH, *Diffractometer Control Program*, Vol. 1.06 (Darmstadt, Germany, 1997).
[10] STOE and Cie GmbH, *X-RED 1.07, Data Reduction for STADI4 and IPDS* (Darmstadt, Germany, 1996).
[11] STOE and Cie GmbH, *X-SHAPE 1.03, Crystal Optimization for Numerical Absorption Correction* (Darmstadt, Germany, 1997).
[12] V. Petricek, M. Dusek, and L. Palatinus, *Jana2000, The Crystallographic Computing System* (Institute of Physics, Praha, Czech Republic, 2000).
[13] S. V. Smaalen, L. Palatinus, and M. Schneider, Acta Crystallogr., Sect. A: Found. Crystallogr. **59**, 459 (2003).
[14] C. J. Gilmore, Acta Crystallogr., Sect. A: Found. Crystallogr. **52**, 561 (1996).
[15] R. Y. De Vries, W. J. Briels, and D. Feil, Acta Crystallogr., Sect. A: Found. Crystallogr. **50**, 383 (1994).
[16] L. Palatinus and S. van Smaalen, Acta Crystallogr., Sect. A: Found. Crystallogr. **58**, 559 (2002).
[17] M. Sakata and M. Sato, Acta Crystallogr., Sect. A: Found. Crystallogr. **46**, 263 (1990).
[18] K. Tsuda and K. Tanaka, Acta Crystallogr., Sect. A: Found. Crystallogr. **55**, 939 (1999).
[19] K. Tanaka and T. Lehmpfuhl, Jpn. J. Appl. Phys. **11**, 1755 (1972).
[20] L. Reimer, *Transmission Electron Microscopy*, Springer Series in Optical Sciences Vol. 36, 2nd ed. (Springer, Berlin, 1989).

[21] N. W. Ashcroft, N. D. Mermin, *Solid State Physics* (Saunders College Publishing, Philadelphia, 1996).
[22] E. Kirkland, *Advanced Computing in Electron Microscopy* (Plenum Press, New York, 1998).
[23] P. Hohenberg and W. Kohn, Phys. Rev. **136**, B864 (1964).
[24] W. Kohn and L. J. Sham, Phys. Rev. **140**, A1133 (1965).
[25] (a) X. Gonze, J.-M. Beuken, R. Caracas, F. Detraux, M. Fuchs, G.-M. Rignanese, L. Sindic, M. Verstraete, G. Zerah, F. Jollet, M. Torrent, A. Roy, M. Mikami, Ph. Ghosez, J.-Y. Raty, and D. C. Allan, Comput. Mater. Sci. **25**, 478 (2002); (b) X. Gonze, G.-M. Rignanese, M. Verstraete, J.-M. Beuken, Y. Pouillon, R. Caracas, F. Jollet, M. Torrent, G. Zerah, M. Mikami, Ph. Ghosez, M. Veithen, J.-Y. Raty, V. Olevano, F. Bruneval, L. Reining, R. Godby, G. Onida, D. R. Hamann, and D. C. Allan, Z. Kristallogr. **220**, 558 (2005); (c) the ABINIT code is a common project of the Université Catholique de Louvain, Corning, Incorporated, and other contributors (URL http://www.abinit.org).
[26] S. Goedecker, M. Teter, and J. Hutter, Phys. Rev. B **54**, 1703 (1996).
[27] O. Dieguez, S. Tinte, A. Antons, C. Bungaro, J. B. Neaton, K. M. Rabe, and D. Vanderbilt, Phys. Rev. B **69**, 212101 (2004).
[28] K. Koepernik and H. Eschrig, Phys. Rev. B **59**, 1743 (1999).
[29] I. Opahle, Ph.D. thesis, TU Dresden, 2001; H. Eschrig, M. Richter, and I. Opahle, in *Relativistic Electronic Structure Theory—Part II: Applications*, edited by P. Schwerdtfeger (Elsevier, Amsterdam, 2004), p. 723.
[30] J. P. Perdew and Y. Wang, Phys. Rev. B **45**, 13244 (1992).
[31] J. P. Perdew, K. Burke, and M. Ernzerhof, Phys. Rev. Lett. **77**, 3865 (1996).
[32] A. Ormeci and H. Rosner, PBE-GGA is recently implemented in FPLO, versions 5.00-18 and 5.00-19, but not yet available in the distributed copies.
[33] R. Bader, *Atoms in Molecules: A Quantum Theory* (Oxford University Press, New York, 1990).
[34] E. C. Subaro, Ferroelectrics **5**, 267 (1973).
[35] P. Ghosez, Ph.D. thesis, Universite Catholique de Louvain, 1997.
[36] A. Weickenmeier and H. Kohl, Acta Crystallogr., Sect. A: Found. Crystallogr. **47**, 590 (1991).
[37] J. M. Cowley and A. F. Moodie, Acta Crystallogr. **10**, 609 (1957).
[38] H. Lichte, M. Reibold, K. Brand, and M. Lehmann, Ultramicroscopy **93**, 199 (2002).